

Solar active region scaling laws revisited

Guilherme A. L. Nogueira¹, Robertus Erdélyi^{1,2,3}, Ruihui Wang^{4,5}, and Kristof Petrovay¹

¹Dept. of Astronomy, Institute of Physics and Astronomy, ELTE Eötvös Loránd University, Budapest, Hungary

²Gyula Bay Zoltán Solar Observatory (GSO), Hungarian Solar Physics Foundation (HSPF), Gyula, Hungary

³Solar Physics and Space Plasma Research Centre, School of Mathematical and Physical Sciences, University of Sheffield, UK

⁴School of Space and Earth Sciences, Beihang University, Beijing, P. R. China

⁵Key Laboratory of Space Environment Monitoring and Information Processing of MIIT, Beijing, P. R. China

e-mail: k.petrovay@astro.elte.hu

February 17, 2026

ABSTRACT

Context. The systematic variation of solar active region (AR) properties with their magnetic flux has been the subject of numerous studies but the proposed scaling laws still vary rather widely.

Aims. A correct representation of these laws and the deviations from them is important for modelling the source term in surface flux transport and dynamo models of space climate variation, and it may also help constrain the subsurface origin of active regions.

Methods. Here we determine active region scaling laws based on the recently constructed ARISE active region data base listing bipolar ARs for cycle 23, 24 and 25.

Results. For the area A , pole separation d and tilt angle γ we find the following scalings against magnetic flux Φ and heliographic latitude λ : $A \propto \Phi^{0.84}$, $\langle d \rangle = 3.32 \log(\Phi/\Phi_0)$, and $\langle \gamma \rangle \approx 28.62 \sin \lambda$, with $\Phi_0 = 1.6 \times 10^{20}$ Mx. Residuals from these relations are also modelled. These scaling relations are recommended for use in space climate research for the modelling of future data or missing past data, as well as for the identification of candidate rogue ARs. We confirm that the tilt angle distribution of non-Hale ARs shows a significant excess at low tilts (anti-Hale ARs). In contrast to earlier studies we show that neither the anti-Hale ARs nor non-Hales in general follow Joy's law: instead, their tilt angle distribution is best represented by vanishing mean tilt.

Conclusions. These results are most easily reconciled with a scenario where the AR flux loops originate in the deep convective zone or below, gaining tilt during their rise under the action of the Coriolis force. A small fraction of the loops is subjected to extreme, intermittent torques resulting in either very large tilts or anti-Hale orientation. Anti-Hale ARs are suggested to be fully curled \square -loops or 'XO-loops', and their excess is caused by a simple mechanical effect, as the contact of their legs increases resistance against further deformation by the torque.

Key words. Sun – Dynamo – Magnetic field – Solar Cycle

1. Introduction

Solar active regions (ARs) are strongly magnetized regions of the solar atmosphere, formed by the emergence of magnetic flux bundles from the subsurface layers (van Driel-Gesztelyi & Green 2015; Fan 2021). Their size can vary in a broad range. From a physical point of view the relevant parameter characterizing their size is the magnetic flux contained in the emerging flux tube. As each emerged field line intersects the surface twice, this flux can be approximated as half the total amount of unsigned magnetic flux integrated over the photospheric area of the AR. This flux measure Φ will generally depend on time (due to flux emergence and cancellation across the neutral line) and on the definition of the AR boundary.

The distribution of AR flux over the solar surface may vary. Hence, other measures of AR size such as sunspot area or plage area may not scale completely linearly with Φ . In addition, the emergence process typically results in a bipolar structure consisting of two opposite polarity flux patches, of mean area A . The line connecting the weighted mean positions of these patches is characterized by its length, the pole separation d , and by its tilt angle γ to the azimuthal direction.

How different AR characteristics, in particular A , d and γ , scale with Φ has been the subject of numerous studies. Due to the large intrinsic scatter in AR properties very large samples are

needed to draw statistically robust conclusions. A further complicating factor is that all parameters vary with time during the evolution of an AR, and further parameters such as heliographic latitude λ or solar cycle phase and amplitude may also come into play. As a result, despite numerous studies, firm quantitative conclusions regarding the form of the scaling laws are still not available.

Nevertheless, determining or at least constraining the scaling laws would be important for several reasons. Firstly, these relations hold important clues for the originating depth and emergence mechanism of the subsurface magnetic flux tubes giving rise to ARs (Fan 2021). Second, surface flux transport models widely used to compute the evolution of the Sun's large scale magnetic field include ARs as a source term (Yeates et al. 2023). This source often needs to be modelled to account for missing data or future evolution: it is clearly important for any such model to be as realistic as possible. Finally, as it has been realised that the Sun's axial dipole moment at the end of a solar activity cycle is a good precursor of the amplitude of the next cycle (Petrovay 2020) and this dipole moment results from the summed contributions of individual ARs, AR scaling laws allowing the calculation of these contributions for a given distribution of ARs in time, latitude and flux have an important role in solar cycle prediction.

One widely accepted assumption concerning the scaling laws, supported (or at least not contradicted) by observational data is that the tilt angle γ is primarily determined by heliographic latitude λ (Joy's law), while the area A and the pole separation d scale with the size of active regions Φ . All these relationships are increasing, but regarding their form (e.g. value of exponent, if modelled as a power law) there is considerable disagreement.

Simple power law scalings are most often considered:

$$A = C_A \Phi^k \quad d = C_d \Phi^m \quad \gamma = C_\gamma (\sin \lambda)^n \quad (1)$$

where C_A , C_d and C_γ are constants. For the exponents, the values $k = 1$, $m = 0.5$ and $n = 1$ are most often suggested. Detailed analyses based on observational data, however, often yield rather different values and even the form of the suggested scaling laws is in doubt in some cases. (See detailed discussions with references below, in Section 3.)

Motivated by the newly acquired importance of AR scaling laws for space climate prediction, in this paper we make a new attempt at constraining the scaling laws based on a recently constructed AR database. Section 2 presents this input data set and its pre-processing to derive the AR parameters under study. Section 3 presents the resulting scaling laws and the distribution of the residuals from these laws, first for the whole data set, then for the non-Hale regions. Section 4 discusses the implications of these findings; finally, Section 5 concludes the paper.

2. Data

2.1. Sample

Our input data were taken from the recently constructed ARISE database¹ of solar active regions. ARISE is a recently constructed database containing basic parameters of bipolar solar active regions, extracted from SOHO/MDI and SDO/HMI synoptic magnetic maps. During the construction of ARISE, ARs were detected based on morphological operations and region growing and their properties were extracted automatically by an algorithm, applying a bipolarity condition and a size threshold. For details the reader should consult the publication describing the database (Wang et al. 2023).

For each AR, parameters of the Northern (positive) and Southern (negative) magnetic polarity parts (here denoted by subscripts N and S) are listed separately in the catalogue.² These listed parameters include heliographic latitude (λ_N , λ_S), longitude (ϕ_N , ϕ_S), area (A_N , A_S) and magnetic flux (Φ_N and Φ_S).

The database is regularly updated, i.e. it is a "living" database. The data used for this study are the version where recurrent ARs have been removed (Wang et al. 2024). This covers the period from Carrington Rotation (CR) 1909 to 2290 (May 1996 - October 2024), corresponding to Solar Cycles 23, 24 and the first half of cycle 25. The total sample is composed of 3005 bipolar ARs.

2.2. Quantities under study

From the data listed in the database for each AR we analyze the relationships between the following quantities.

Φ : Total absolute magnetic flux, calculated as $\Phi = (|\Phi_N| + |\Phi_S|)/2$ where Φ_N and Φ_S are the magnetic fluxes in the northern and southern polarity parts of the AR, respectively. Φ is given in units of maxwell [Mx], or, in some cases SFU (solar flux unit, Sheeley 1966). 1 SFU = 10^{21} Mx.

A : Total area per polarity, calculated as $A = (A_N + A_S)/2$ where A_N and A_S are the areas of the northern and southern polarity parts of the AR, respectively. A is given in units of microhemisphere [MSH].

λ : Heliographic latitude $\lambda = (\lambda_N + \lambda_S)/2$, given in degrees.

d : Pole separation, i.e. the distance between the centers of the N and S polarity parts, calculated from the spherical cosine theorem

$$\cos d = \sin \lambda_N \sin \lambda_S + \cos \lambda_N \cos \lambda_S \cos(\phi_N - \phi_S) \quad (2)$$

where ϕ and λ are heliographic longitude and latitude, respectively. d is given in [heliocentric] degrees.

γ : Tilt angle, defined as

$$\gamma = \arctan \frac{\lambda_S - \lambda_N}{\cos \lambda (\phi_N - \phi_S)} \quad (3)$$

Note that this formula is a Euclidean approximation to the azimuth of the direction of the trailing (lower heliographic longitude) polarity from the vantage point of the leading (higher longitude) polarity, the azimuth being measured northwards from east. The formula does not distinguish ARs following Hale's polarity rules from those opposing it (non-Hale ARs). In our processing of the data non-Hale regions have been flagged based on the heliographic longitudes of the polarities, and they were separated in some studies. γ is expressed in degrees.

As the typical sign of γ is opposite on the two hemispheres in accordance with Joy's law, we also introduce the alternative form

$$\gamma_J = \gamma \cdot \text{sgn } \lambda \quad (4)$$

which has the same sign on both hemispheres for ARs adhering to Joy's law. Thus, $\langle \gamma_J \rangle$ measures overall adherence to Joy's law in a given population; $\langle |\gamma| \rangle$ characterizes the preferred azimuthal orientation (East–West vs. North–South); while $\langle \gamma \rangle$ typifies hemispheric asymmetry.

2.3. Cycle assignment and flagging of non-Hale regions

For each AR in the database, adherence to Hale's polarity rules was indicated by a flag taking the value +1 (Hale) or -1 (non-Hale). The flag was automatically set to the value $\text{sgn} \{(\phi_N - \phi_S) \lambda [(n_C \bmod 2) - 0.5]\}$, where n_C is the cycle number.

Hale's polarity rule for bipolar ARs, as formulated above, states that the leading (higher heliographic longitude) polarity is normally positive for odd-numbered cycles in the Northern hemisphere, and it alternates between hemispheres and cycles. To judge the adherence of any particular AR to the rule, correct cycle assignment is clearly important.

In a first approximation, cycle assignment was based on the date of the observation, using the official starting date of each cycle as given in the SIDC/SILSO database.³ As, however, cycles are known to overlap by up to 2 years, this first cycle assignment was manually corrected for high latitude ARs in the last 20 CRs

¹ <https://github.com/Wang-Ruihui/A-live-homogeneous-database-of-solar-active-regions>

² Note for readers less familiar with magnetic data: Northern and Southern polarity here refer to the directionality of magnetic field lines and they are not related to heliographic latitude.

³ <https://www.sidc.be/SILSO/cyclesminmax>

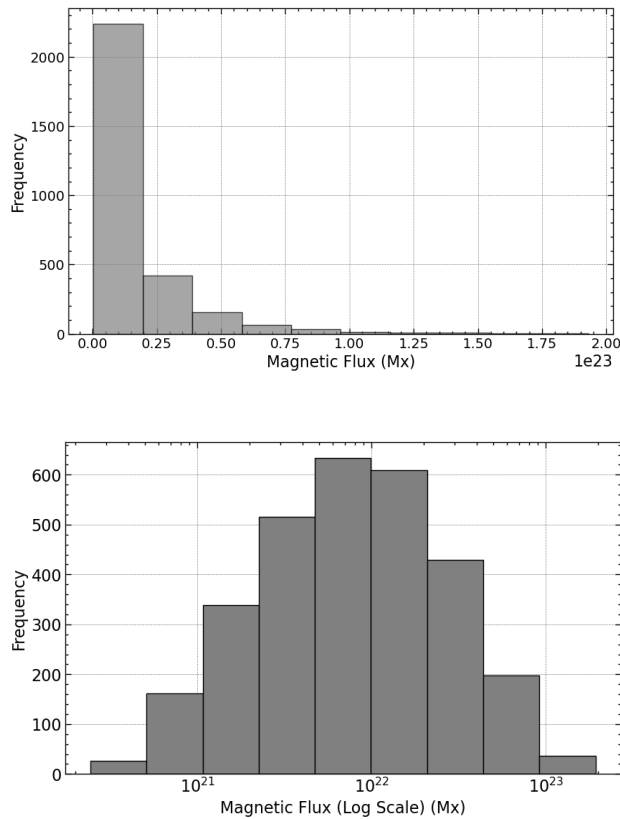


Fig. 1. Histogram of the total flux Φ of active regions on linear (left) and logarithmic (right) scale

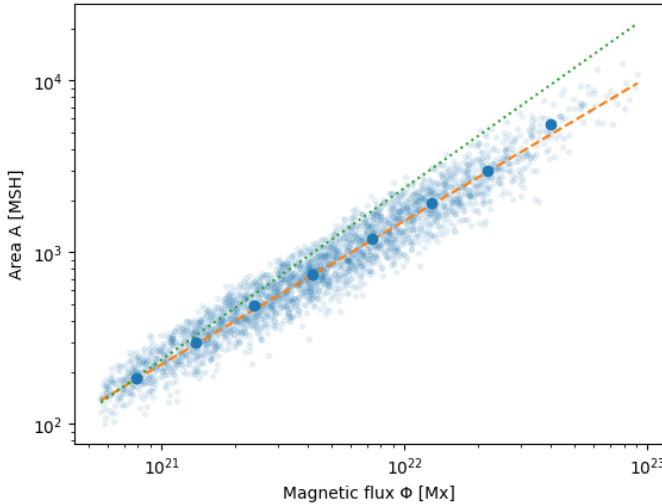


Fig. 2. Plot of active region area A vs. magnetic flux Φ , with power law fits to the medians of the binned data (blue circles with error bars). The dashed line corresponds to the optimal fit; the dotted line shows a linear relationship $A \sim \Phi$ for comparison. Lighter background is a scatterplot of the individual points.

and for low latitude ARs in the first 20 CRs during each cycle. The dividing line between "high" and "low" here lies roughly at $|\lambda| = 15^\circ$ latitude but as the latitudinal distribution in these time periods displays a very clear bimodality, there was no ambivalence in selecting the ill-assigned ARs. The corrected cycle

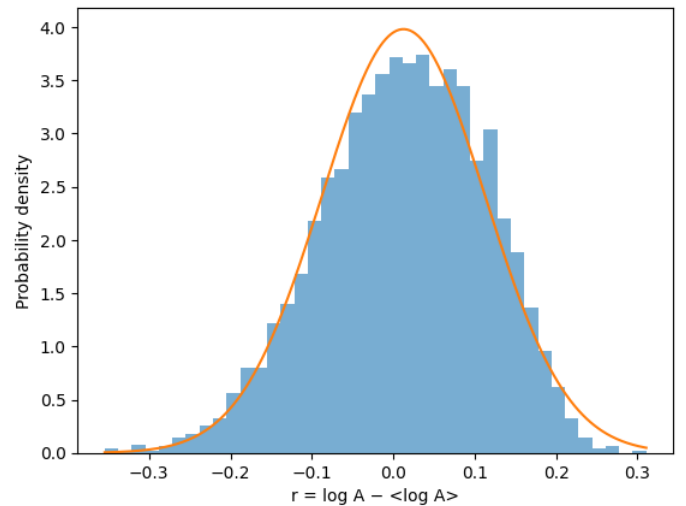


Fig. 3. Histogram of the residuals from the fit in Fig. 2. The solid line is a Gaussian fit.

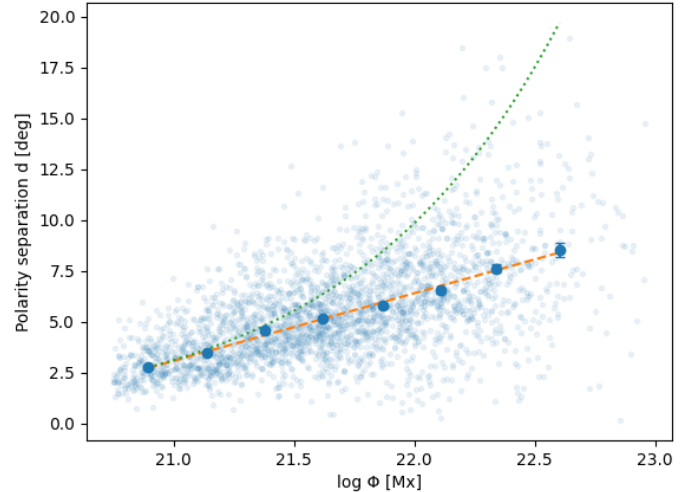


Fig. 4. Plot of the polarity separation d vs. logarithm of active region flux Φ . Median values are plotted for each bin (blue circles with error bars). The dashed line is a linear (i.e. logarithmic) fit. The dotted line shows the scaling $d \sim \Phi^{1/2}$ for comparison. Lighter background is a scatterplot of the individual points.

attributions were also compared with the assignments given by Leussu et al. (2017) wherever possible.

This resulted in manual correction of the cycle assignment for 30 ARs. While this is less than 1 % of the total sample size, it is a much more sizable fraction of the 139 identified non-Hale ARs. Manually correcting cycle assignments is therefore an important step to correctly determine the bulk properties of the non-Hale population.

The overall fraction of non-Hale regions is 4.7 %, which is close to the value of 5.6 % reported by Muñoz-Jaramillo et al. (2021), while it is somewhat less than the ~ 8 % values found by McClintock et al. (2014) and Li (2018). Discrepancies likely originate in differences like inclusion of smaller regions and correction of cycle assignment for cycle overlap.

3. Results

Histograms of the flux values and their logarithms are shown in Fig. 1. These histograms are subject to a heavy bias for

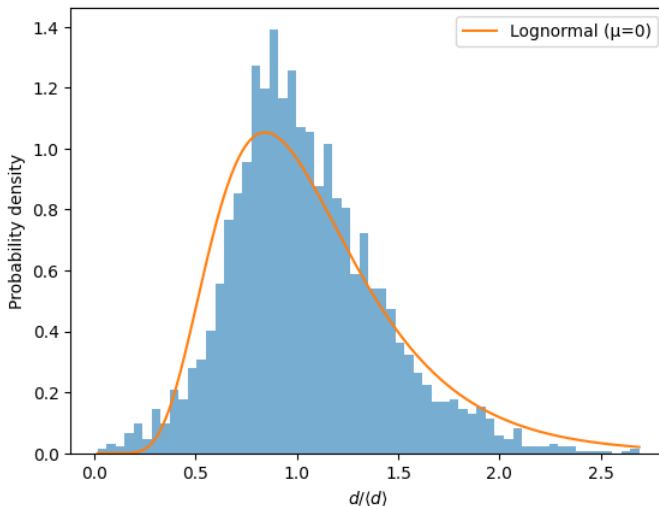


Fig. 5. Histogram of the fractional residuals $d/\langle d \rangle$ relative to the linear fit in Fig. 4. The solid curve is a lognormal fit.

lower fluxes due to the field strength threshold (50 G/30 G in MDI/HMI data), area threshold ($412 \text{ Mm}^2 \simeq 4.2 \text{ MSH}$) and morphological transformations applied during the compilation of the ARISE database. Nevertheless, irrespective of the effects shaping the distribution, it can be seen that the histogram of the flux values is strongly skewed, with a long tail. The histogram of $\log \Phi$, in contrast, is much less skewed. This is in agreement with the known result that the size distribution of larger ARs, less affected by selection effects, is approximately lognormal (Harvey & Zwaan 1993, Seiden & Wentzel 1996, Muñoz-Jaramillo et al. 2015). Hence we opt to group our data into bins equidistant in $\log \Phi$. Nine bins are introduced; the bins have widths of 0.25, except the lowest and highest bins that comprise all ARs with $\log \Phi < 20.75$ and $\log \Phi > 22.5$, respectively. The lowest flux bin, most heavily influenced by the threshold effects, is discarded.

For variables with a non-normal distribution the use of the median is expected to be more robust than using the mean. Hence, for each bin, the median value of the variable studied is calculated. The uncertainty of this value is estimated as $\sigma_i / \sqrt{n_i}$, with n_i the number of values in the bin and σ_i their standard deviations. While this formula is strictly only valid for a normal distribution, the error introduced by this is considered admissible in view of the large extra computational burden that a proper bootstrap estimate would imply. This approximation nevertheless calls for due mental reservation when evaluating fits with a significantly non-Gaussian scatter and resulting in p -values that are not close to either 1 or 0.

3.1. Area vs. flux

For the relation between flux and area, a log–log representation of the results is shown in Fig. 2. A linear regression (dashed) provides a very good representation of the data ($\chi^2 = 1.83$, p -value 0.78):

$$\log A = k \log \Phi + \log C_A \quad (5)$$

with $k = 0.836 \pm 0.005$ and $\log C_A = -15.21 \pm 0.11$. (Recall that Φ is given in units of Mx and A is given in MSH.) The fit corresponds to a power law dependence of the form $A = C_A \Phi^k$ with $C_A = 6.17 \cdot 10^{-16}$, using the same units. The case $k = 1$ (dotted) is clearly excluded.

The histogram of logarithmic residuals from equation 5 is displayed in Fig. 3. Despite a distinct negative skew (skewness -0.28), a Gaussian fit with standard deviation 0.1 provides a reasonable representation of the data. This means that for a bipolar region of magnetic flux Φ the logarithm of the area of the individual polarity patches is best represented as $\log A = \langle \log A \rangle + r_A$ where $\langle \log A \rangle = k \log \Phi + \log C_A$ and r_A is a Gaussian random variable with standard deviation 0.1.

The analysis was repeated separating individual solar cycles: all cycles were found to follow the scaling (5), without statistically significant deviations.

The power-law scaling found here is in good agreement with the findings of Meunier (2003) who reported $A \sim \Phi^{1/k}$ with $1/k \simeq 1.2$ for the inverse relation. Other previous studies of the relationship between magnetic flux and area in solar active regions all resulted in linear scalings, i.e. $k = 1$ (Sheeley 1966; Wang & Sheeley 1989; van Driel-Gesztelyi & Green 2015; Murskaözy 2024). These studies, however, were mostly limited to sunspots; they did not normally present a statistical test of the goodness of the fits suggested; and the flux estimates used in early studies were rather crude.

It follows from our result that the average field strength $\Phi/A \sim \Phi^{0.16}$. While this is a mild increase, over the two orders of magnitude in flux covered by our sample ($10^{21}\text{--}10^{23}\text{Mx}$) it still implies a factor of two increase in the average field amplitude. Whether this increase is due to a higher fraction of the area covered by spots or to a higher overall plage field strength is unclear. Further research should shed light on this issue.

3.2. Pole separation vs. flux

Fig. 4 plots d against Φ for all ARs in the data base. It is apparent that a logarithmic fit of the form

$$\langle d \rangle = m_d \log(\Phi/\Phi_0) \quad (6)$$

provides a very good description of the data ($\chi^2 = 0.8$, p -value 0.997). The best fit parameters obtained by linear regression are $m_d = 3.32 \pm 0.11$ and $\Phi_0 = 0.16 \text{ SFU}$.

The relation between Φ and d has been considered in a surprisingly low number of studies. Wang & Sheeley (1989), Tian et al. (2003) and Lemerle et al. (2015) all reported a power-law relationship, i.e. $d \sim \Phi^m$, however the exponents obtained varied substantially, values being $m = 0.77$, $m = 0.87$ and $m = 0.42$, respectively. This was based on a direct linear regression fit to an unbinned log–log scatterplot in all cases, and the goodness of the fit was not determined. The high p -value obtained in our analysis clearly shows that a logarithmic fit is superior to the power law fits. We note that a first indication of the logarithmic relationship can also be seen in Fig. 4 of Erofeev & Erofeeva (2023) where, based on white-light images, the plotted relation between the logarithm of the total sunspot area in a sunspot group vs. the pole separation of clearly bipolar groups is not too far from linear.

Fig. 5 presents the histogram of the fractional residuals $r_d = d/\langle d \rangle$ relative to the mean law given by eq. 6. A lognormal fit is found to be a reasonably good representation of the data. Accordingly, for a bipolar region of magnetic flux Φ the pole separation may be best represented as $d = r_d \cdot \langle d \rangle$ where $\langle d \rangle = m_d \log(\Phi/\Phi_0)$ as above and $\log(r_d)$ is a normally distributed random variable, with standard deviation 0.41.

Table 1. Bulk characteristics of the tilt for the whole sample, and for non-Hale ARs

| | Tilt values [°] | | |
|---|--------------------------|----------------------------|----------------------------|
| | $\langle \gamma \rangle$ | $\langle \gamma_J \rangle$ | $\langle \gamma \rangle$ |
| all ARs ($N = 3005$): | | | |
| median | -0.50 | 7.95 | 14.09 |
| mean | -0.62 | 6.57 | 18.48 |
| st. dev. σ | 24.94 | 24.07 | 16.76 |
| error σ / \sqrt{N} | 0.45 | 0.44 | 0.31 |
| non-Hale ARs ($N = 139$): | | | |
| median | 3.38 | -1.65 | 33.06 |
| mean | 0.35 | -2.45 | 37.66 |
| st. dev. σ | 47.08 | 47.02 | 28.07 |
| error σ / \sqrt{N} | 3.99 | 3.99 | 2.38 |

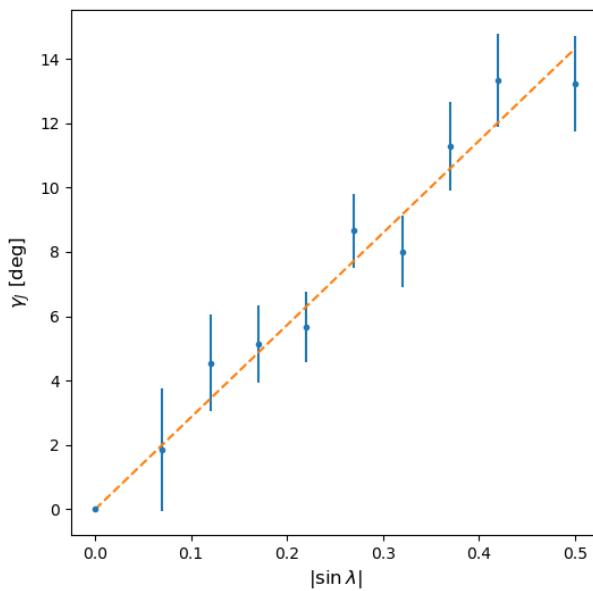


Fig. 6. Plot of the tilt angle following Joy's convention, γ_J vs. sine latitude for the complete sample. The dashed line is a homogeneous linear fit.

3.3. Tilt vs. latitude (Joy's law)

Bulk characteristics of the tilt distribution are summarized in Table 1. The complete sample shows a clear preference for a tilt of $\gamma_J \sim 7^\circ$, with the leading pole positioned closer to the equator, in accordance with Joy's law. The numbers in the table align well with the findings of Qin et al. (2025) and they place the ARISE sample among the higher-tilt ones, as discussed by Erofeev & Erofeeva (2023). This is in line (Wang et al. 2015) with the relatively high lower size thresholds applied during the compilation of the database, as well as the selection of ARs with a clearly bipolar structure and good polarity balance. Note that discrep-

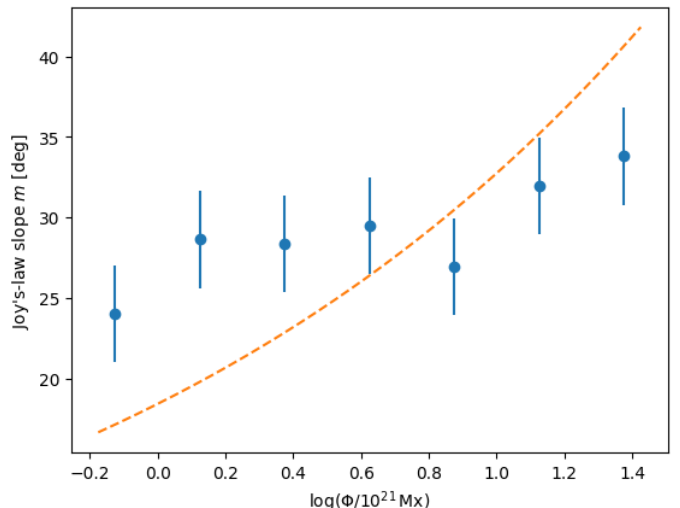


Fig. 7. Slope of Joy's law determined for subsamples in different flux bins plotted against $\log \Phi$. The dashed line is an optimal fit of the form $m_J \sim \Phi^{1/4}$, clearly inconsistent with the data.

ancies between data sets may also be related to the presence of magnetic tongues in plage structure (Poisson et al. 2020).

Hemispheric asymmetry, as characterized by $\langle \gamma \rangle$, is not significant.

In contrast to area and pole separation, the tilt angle has been known to be primarily determined by heliographic latitude rather than flux (Joy's law). To study this relation, we choose $\sin \lambda$ as independent variable. This is motivated by the consideration that Joy's law most plausibly originates from the Coriolis force which scales with $\sin \lambda$. Nine bins are introduced; the bins have widths of 0.05, except the lowest and highest bins that comprise all ARs with $|\sin \lambda| < 0.1$ and $|\sin \lambda| > 0.45$, respectively.

Figure 6 presents the binned data with the Southern hemisphere folded over the Northern one, i.e. as a function of $|\sin \lambda|$. A simple one-parameter linear fit of the form

$$\langle \gamma_J \rangle = m_J \sin \lambda \quad m_J = 28.62 \pm 1.44 \quad (7)$$

is clearly a perfectly good representation of the data ($\chi^2 = 0.54$, p -value 0.9998). We are thus unable to confirm occasional claims in the literature (McClintock & Norton 2013; Erofeev & Erofeeva 2023) of various nonlinearities in the shape of Joy's law.

Separating the data by hemisphere or by solar cycle, no statistically significant differences in the value of the coefficient in Joy's law were found. Our results for cycles 23 and 24 agree with the findings of Will et al. (2024) in that the value of m_J is higher in cycle 23 but the difference is not significant. The form of our fitting function, forced to go through the origin may have a role in the lack of hemispheric asymmetry in our study. As recently pointed out by Zeng et al. (2024), the hemispheric asymmetry apparent in some studies is mostly due to low-latitude regions, and this would only show up when a non-zero intercept is allowed for.

While the primary determinant of the tilt is clearly the latitude, some theoretical and empirical studies suggest that magnetic flux or AR size may have a secondary role (D'Silva & Howard 1993; Fan et al. 1994; Fisher et al. 1995; Sreedevi et al. 2024; Qin et al. 2025). In Fig. 7 we plot the value of the slope m_J for subsamples divided into flux bins, as used in the previous sections. (The top and bottom flux bins are not shown as here some latitude bins contain too few points for reliable fits.) The plot is

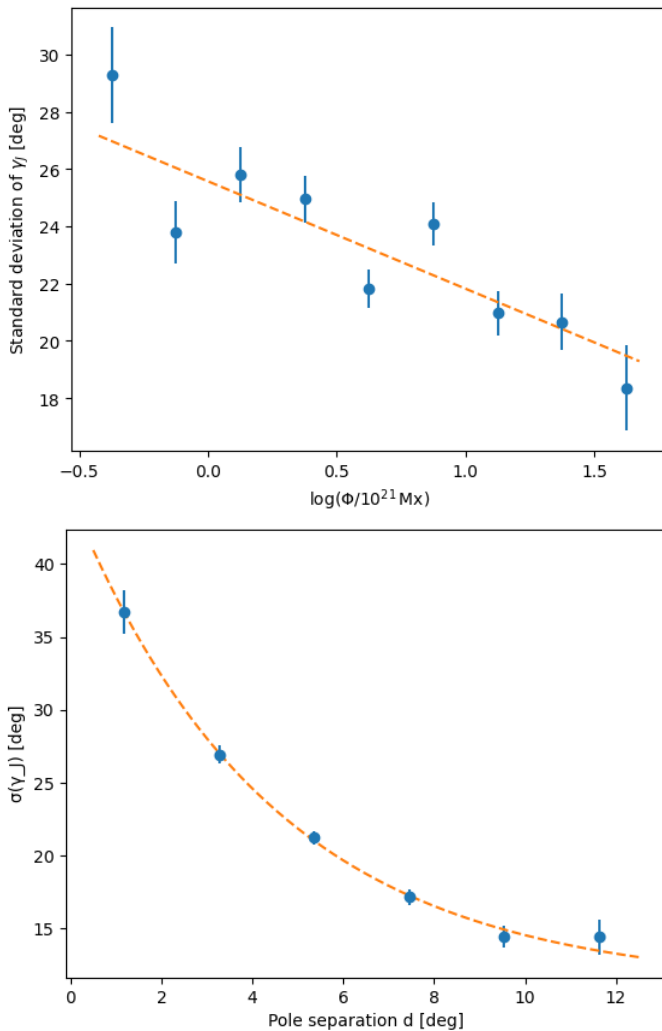


Fig. 8. Plot of the standard deviation of tilt angles γ_J vs. magnetic flux (left) and pole separation (right). The dashed lines are linear and exponential fits, respectively.

strongly suggestive of an increasing trend, but the null hypothesis of no dependence cannot be discarded with more than $\sim 1\sigma$ confidence, while the classic theoretical prediction $m_J \sim \Phi^{1/4}$ (Fan et al. 1994) is clearly inconsistent with the data. If only three flux bins are used (with divisions at 2 and 7 SFU), the resulting Joy slopes in order of increasing flux are $m_J = 26^\circ.1$, $28^\circ.4$ and $33^\circ.1$, respectively. The increasing trend is again suggestive, while the null hypothesis cannot be discarded at a confidence level much better than 1σ . (This also illustrates the low sensitivity of our findings to the choice of binning, not demonstrated here in each and every case.)

These inconclusive results rhyme with contradictory results in previous studies, some of which reported no correlation or even negative correlations of tilt with flux (Kosovichev & Stenflo 2008; McClintock & Norton 2016; Jha et al. 2020).

The standard deviation of the tilt values, on the other hand, displays a much clearer trend with magnetic flux (Fig. 8), significant at 6σ . A linear best fit results in

$$\sigma_J = a + b \log(\Phi[\text{SFU}]) \quad \text{with} \quad (8)$$

$$a = 25.57 \pm 0.51^\circ \quad \text{and} \quad b = 3.75 \pm 0.61^\circ$$

Given our above finding $d \sim \log \Phi$, we also construct a plot of σ_J vs. d (Fig. 8, right panel). The alignment of the points

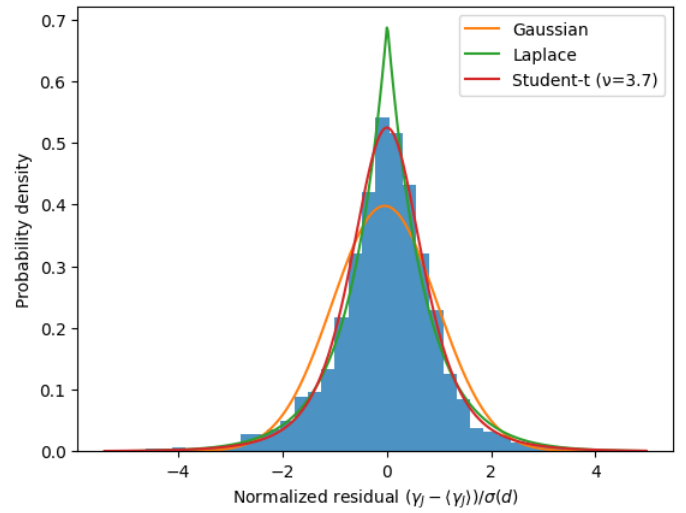


Fig. 9. Histogram of normalized residuals around Joy's law. Optimally fitted Gaussian, Student's t and Laplace distributions are shown for comparison.

becomes even tighter in this case, indicating that the geometry of the rising loop plays a more direct role in regulating deviations from Joy's law. An exponential fit is found to be a convincing description (p -value 0.73) of the relation:

$$\sigma_J = \sigma_\infty + A \exp(-d/d_0) \quad \text{with} \quad (9)$$

$$\sigma_\infty = 11.0 \pm 1.7 \quad A = 33.5 \pm 1.9^\circ \quad d_0 = 4.4 \pm 0.7^\circ$$

Note that the stronger dependence of the scatter on d may at least partly be caused by a simple geometrical effect. For an uncertainty σ_p in the determination of the pole position, the error in tilt determination will be σ_p/d , decreasing with separation.

Note that the possibility that the poorer alignment of the scatter against flux may be due to lower precision of the flux determination cannot be completely discarded. However, we do not consider this possibility highly likely, given that flux values in the ARISE catalogue were carefully cross-checked comparing MDI vs HMI data and against other catalogues (Wang et al. 2023). Furthermore, Fisher et al. (1995) report a similarly tight relation between d and tilt scatter even though their d values were determined from white light images only, implying significantly larger uncertainties. Finally, we note that Stenflo & Kosovichev (2012) report a much stronger dependence of tilt scatter on Φ but only for flux values in the range 0.1–1 SNU, below that studied here.

It remains to determine the form of the distribution of the residuals around Joy's law. The decreasing trend of scatter around the law, equation (9), suggests to use normalized residuals $r_J = (\gamma_J - \langle \gamma_J \rangle)/\sigma_J$. The histogram of the r_J values using equation (9) for σ_J is displayed in Fig. 9. Clearly, with this normalization, the full sample collapses onto a nearly universal distribution.

To model this distribution, we first attempt to fit a Gaussian, which would be the natural expectation for tilt scatter resulting from random convective buffeting during flux emergence. Many such independent convective kicks should naturally result in a Gaussian distribution by virtue of the central limit theorem of probability theory. The Gaussian fit, however, can be rejected with a very high confidence (p -value of $3 \cdot 10^{-8}$ based on a Kolmogorov–Smirnov test). Even by visual inspection, the distribution is distinctly non-Gaussian and leptokurtic, with a strong

peak and extended tails (excess kurtosis +2.8). The high excess kurtosis is the hallmark of an intermittent stochastic perturbing process where most instances are only slightly perturbed (the strong peak), while in a small fraction of instances a single large perturbation results in large deviations (the tail). Standard methods in statistical physics to model such leptokurtic distributions resulting from intermittent processes include a double exponential (a.k.a. Laplace) distribution or Student's *t*-distribution. The Laplace distribution fits our data only marginally (*p*-value 0.067), while a satisfactory overall match is provided by Student's *t*-distribution with 3.7 degrees of freedom (*p*-value 0.18). This agrees with the findings of Muñoz-Jaramillo et al. (2021) that a *t*-distribution with 3.45 degrees of freedom represents well the (unnormalized) tilt residuals.

The presence of extended tails thus indicates that fluctuations are governed by intermittent, impulsive perturbations to the emerging flux tubes, rather than many small, independent Gaussian kicks. This type of distribution may be expected from sporadic convective buffeting, pre-existing magnetic structures, or episodic vortical forcing during emergence.

The actual histogram of normalized residuals, however, has a considerable skewness of -0.4 . From visual inspection of Fig. 9 this asymmetry is primarily located in the tails, where negative residuals are more common than the fitted *t*-distribution, while positive residuals are less common. This seems to suggest that AR flux tubes subjected to excessive disturbance prior to emergence tend to become completely oblivious of Joy's law, their tilt distribution becoming more symmetrical to the equator.

In summary, we suggest that for a bipolar region of magnetic flux Φ emerging at latitude λ the tilt angle γ_J is best represented as $\langle \gamma_J \rangle + r_J \sigma_J$ where r_J is a random variable with a distribution described by Student's *t*-distribution of 3.7 degrees of freedom, and σ_J is obtained from equation (9) [or alternately from (8), in which case a *t*-function with 2.9 degrees of freedom is to be used]. For applications where an accurate representation of the tails of the distribution matters, accounting for the skewness by suppressing [amplifying] the positive [negative] tail of the distribution may be considered.

3.4. Non-Hale regions

The bulk properties of non-Hale ARs are in some respects rather different from the total sample. This is evident from the lower panel of Table 1. While still hemispherically symmetric, this subsample shows no sign of a preferred tilt. At the same time, $\langle |\gamma| \rangle$ is significantly below 45° , indicating a clear preference for East–West orientation. This preference is further borne out in Fig. 10: there is a clear excess of non-Hale ARs in the two low-tilt bins.

These results corroborate previous findings (McClintock et al. 2014; Muñoz-Jaramillo et al. 2021) that, rather than being the tail of a single distribution, at least some non-Hale ARs form a distinct population with preferred East–West orientation. While individual ARs cannot be uniquely assigned to either of these two subsets, Fig. 10 suggests that further restricting our sample to ARs with tilt $|\gamma| < 20^\circ$ will yield a statistically much clearer sample of anti-Hales. For clarity, we will henceforth simply refer to non-Hale ARs with $|\gamma| < 20^\circ$ as “anti-Hale regions”, while other non-Hale regions with higher tilts will be referred to as “flipped Hale regions”. The latter name already implies the tacit assumption that high-tilt non-Hale ARs simply form the extreme tail of the tilt distribution of Hale ARs, while a similar assumption is not made for the anti-Hale ARs at this stage. Nevertheless, here we may already hint that in our later discussion

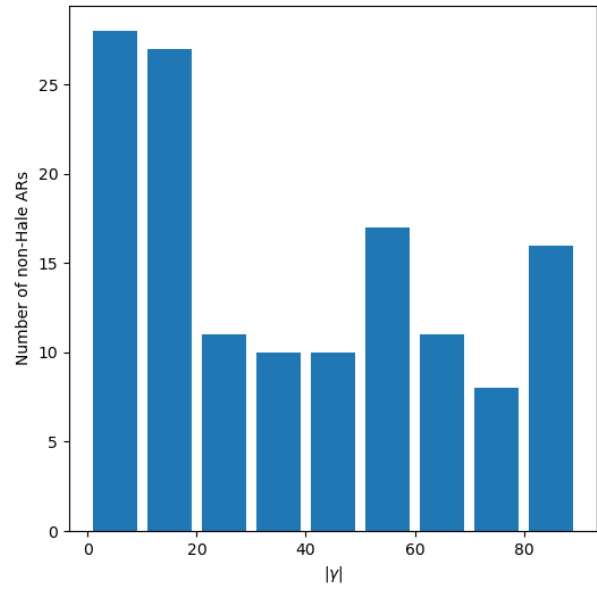


Fig. 10. Histogram of $|\gamma|$ for non-Hale regions in 10° bins. A preference for East–West orientation is clearly visible.

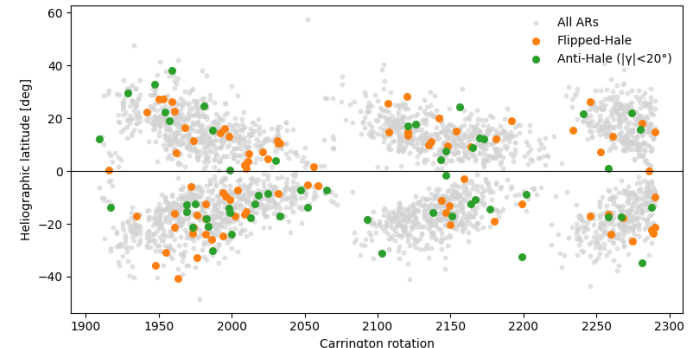


Fig. 11. Butterfly diagram for the two subsets of non-Hale regions against the background of all ARs (in grey).

(Sect. 4.2) anti-Hale ARs will be suggested to be just a special subclass of flipped Hale regions, where the loop legs have come in contact —cf. Fig. 14. The number of anti-Hale ARs in the lowest two bins in the histogram is 56, comparable to the number of putative “flipped-Hale” regions in the other bins, which is 83.

The butterfly diagram of the two types of non-Hale regions is displayed in Fig. 11 against the background of all ARs. No systematic differences between these populations can be discerned. In particular, it is important to note that non-Hales do not seem to be more concentrated to low latitudes than the general population. Diffusive cancellation of oppositely oriented toroidal fields across the equator (Cameron & Schüssler 2016) might in principle lead to a mix of oppositely oriented intermittent field structures at low latitudes; this, however, does not seem to play a major role in the origin of the anti-Hale population. Similarly, while a corrugated magnetic equator may result in some Hale ARs appearing on the “wrong side” of the geometrical equator and being flagged as anti-Hales, the number of anti-Hale regions close to the equator is a very small fraction of the total. The clearly ev-

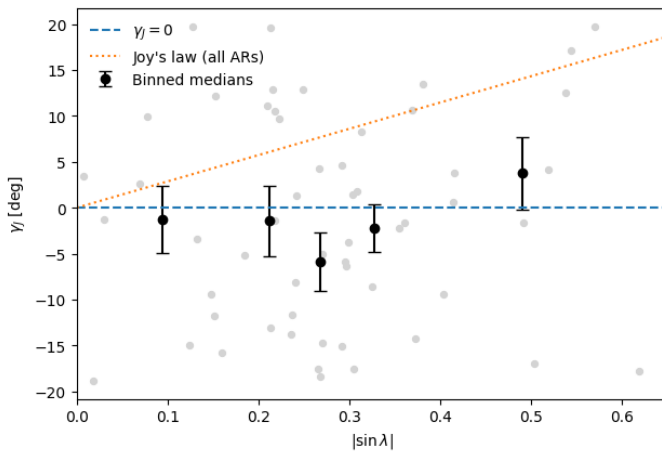


Fig. 12. Tilt vs. sine latitude for the anti-Hale regions. The distribution is consistent with zero mean tilt and no dependence on latitude (blue dashed line). Joy's law for the full AR population is shown as a dotted orange line for comparison.

Table 2. Bulk size parameters for the two subcategories of non-Hale regions. Values for the full sample are shown for comparison.

| | $\langle \log \Phi [\text{SFU}] \rangle$ | $\langle d \rangle [\text{deg}]$ |
|--|--|----------------------------------|
| anti-Hale ARs | | |
| $(\gamma < 20^\circ, N = 56)$: | | |
| median | 0.43 | 4.16 |
| mean | 0.39 | 4.41 |
| st. dev. σ | 0.51 | 2.46 |
| error σ/\sqrt{N} | 0.07 | 0.33 |
| flipped Hale ARs | | |
| $(\gamma > 20^\circ, N = 83)$: | | |
| median | 0.60 | 3.09 |
| mean | 0.57 | 3.30 |
| st. dev. σ | 0.58 | 3.30 |
| error σ/\sqrt{N} | 0.06 | 0.36 |
| all ARs ($N = 3005$) | | |
| median | 0.60 | 4.86 |
| mean | 0.58 | 5.21 |
| st. dev. σ | 0.53 | 2.58 |
| error σ/\sqrt{N} | 0.01 | 0.05 |

idenced presence of an excess anti-Hale population is therefore nontrivial and requires explanation.

To shed more light on this issue, we next repeat our previous analyses on the anti-Hale population. In view of the limited number of points, the number of flux bins used is now reduced to 5, and bins with equal number of points are used.

Fig. 12 shows the distribution of tilt against latitude for the anti-Hale regions. The distribution is consistent ($\chi^2 = 5.42$, p -value 0.37) with zero mean tilt and no dependence on latitude. In contrast, the form (7) of Joy's law, valid for the full AR population, can be rejected with a high degree of confidence ($\chi^2 = 50.7$,

p -value 10^{-9}). Thus, contrary to some earlier results (Li 2018; Muñoz-Jaramillo et al. 2021) we find that anti-Hales do not follow Joy's law: instead, they tend towards zero mean tilt from the East–West axis. Note that a closer inspection of the data in the earlier studies claiming adherence to Joy's law by anti-Hales (e.g. Fig. 7 and Table 3 in Muñoz-Jaramillo et al. 2021) shows that the statistical significance of those findings was low.

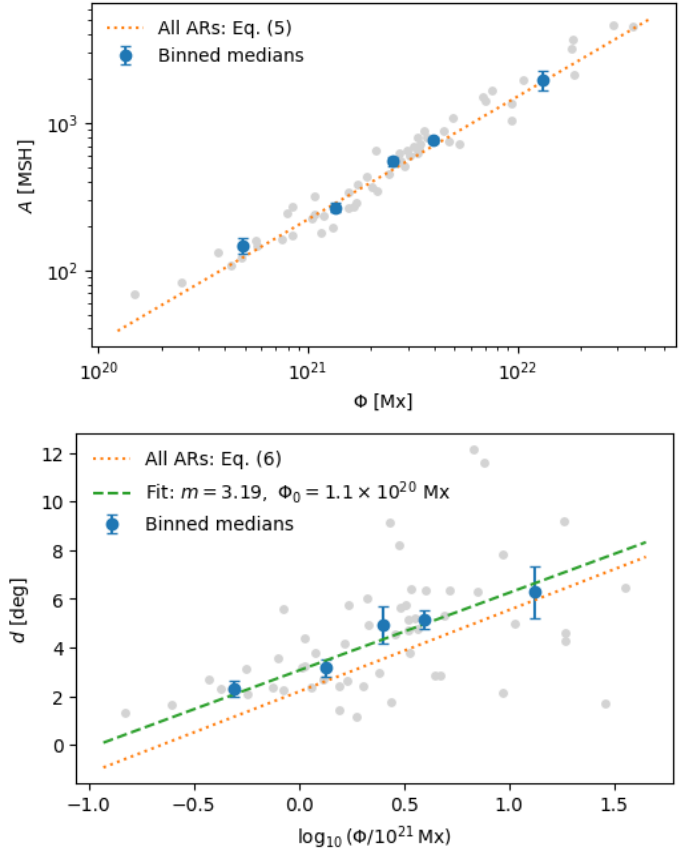


Fig. 13. Scaling laws for the anti-Hale regions. Top: Φ – A relation; bottom: Φ – d relation. The dotted orange lines show the relations for the whole sample, eqs. (5) and (6), respectively, from which the present subsample does not strongly deviate. In the case of the logarithmic Φ – d relation a re-fitting (green dashes) results in only slightly modified parameters.

In view of this highly unusual behaviour of the tilt of anti-Hale ARs it is remarkable to find that in other respects they behave like ordinary bipolar regions. This is borne out by Fig. 13. It is apparent that anti-Hale regions follow both the flux–area relation (5) and the logarithmic d – Φ scaling (6) without major deviations. Indeed, the deviations are insignificant for the Φ – A relation while they are minor for the Φ – d relation where the same logarithmic scaling is found to hold with slightly lower values for the parameters ($m_d = 3.19$ and $\Phi_0 = 0.11$ SFU).

As a side remark, the clear logarithmic Φ – d scaling, similar to the scaling valid for the whole AR population confirms that these anti-Hale regions are not misidentified, i.e. they are not physically unrelated opposite polarity flux patches accidentally lying close to each other, as in this case no such systematic d – Φ relation should be expected.

To what extent can these properties of anti-Hales be extended to the rest of the non-Hale population? A similar analysis (not shown here) shows that the invalidity of Joy's law and lack of tilt is also characteristic of the general non-Hale popu-

lation. Similarly, the robust A – Φ scaling remains unchanged for these regions. The d – Φ relation is complicated by a subtle selection effect, caused by a trend visible in Table 2: non-Hales with tilts higher than 20° have significantly smaller pole separations than the general population, despite having the same typical flux. This trend is clearly related to the marked dependence of scatter around Joy’s law on pole separation, discussed above (Fig. 8). This supports our identification of these ARs as flipped Hale regions: as a consequence of Fig. 8, higher pole separations are underrepresented among ARs of a given flux. Due to the link between flux and pole separation (Sect. 3.2), this bias is expected to decrease towards lower flux values, the net effect being a non-monotonic d – Φ relation for flipped Hale regions.

Table 2 further shows an even more curious trend: in contrast to flipped Hales, anti-Hale regions have substantially lower flux than the general population — yet their pole separation is higher than that of flipped-Hale regions, and about halfway between flipped-Hales and Hales. The differences are significant at a $\sim 2\sigma$ level. An explanation for this curious finding will be offered in Section 4.2 below.

4. Discussion

4.1. Evolutionary effects

Active regions are evolving throughout their life time, implying that all the studied quantities depend on time (van Driel-Gesztelyi & Green 2015, Forgács-Dajka et al. 2021). The AR data listed in the ARISE catalogue were obtained from synoptic maps. On these maps, ARs are captured on the day of their central meridian passage, i.e. at a random instant during their evolution. It is therefore not necessarily trivial to link, e.g., the measured value of the flux Φ to its maximal value Φ_0 , which presumably corresponds to the physically meaningful total magnetic flux in the rising magnetic flux loop. Other parameters like d or γ may not display a maximum in their evolution but some characteristic values corresponding to a certain evolution phase (e.g. when Φ attains its maximum) may still be defined. The question arises to what extent the scaling relations derived above can be considered valid for the more meaningful underlying parameters Φ_0 , d_0 etc.

Fortunately, there is some evidence that the parameter evolution curves of ARs exhibit a certain universality, i.e., for any observable y

$$y = y_0 f_y(t/T) \quad (10)$$

where the AR lifetime $T = f(\Phi_0)$ and the function $f_y(x)$ is a universal average AR evolution curve for the observable y . These average curves were recently determined by Švanda et al. (2025) for different observables up to a time shortly after flux maximum for 36 ARs. The curves are generally consistent with findings from previous studies with narrower focus or smaller samples (Kosovichev & Stenflo 2008; Schunker et al. 2019; Will et al. 2024).

Accepting the universality assumption, the expected value of an observable at a random instant, as measured on synoptic maps, will scale linearly with the characteristic value y_0 :

$$\langle y \rangle = \frac{1}{T} \int_0^T y_0 f_y(t/T) dt = y_0 \int_0^1 f_y(x) dx \quad (11)$$

This suggests that the scalings found in this work may indeed be valid also for the underlying characteristic scales, with a scatter resulting from a combination of evolutionary phase and real physical scatter.

Despite the evidence for a universal average behaviour, some doubts regarding its validity linger, especially in the case of the tilt (McClintock & Norton 2016). Further, more extensive studies of AR evolution are needed to clarify this issue. Studies like Schunker et al. (2020), or the AutoTAB catalogue compiled by Sreedevi et al. (2023) are important steps in this direction.

4.2. The origin of anti-Hale regions

The most plausible, and for a long time the only suggested interpretation of the non-Hale orientation of some observed ARs was that they represent the extreme tails of the distribution of tilt scatter around Joy’s law. In the past ten years, however, with the realization of the existence of a significant, and apparently separate population of low-tilt anti-Hale ARs, an alternative explanation has been promoted (e.g., Stenflo & Kosovichev 2012; Muñoz-Jaramillo et al. 2021). In this scenario, anti-Hale regions would result from an oppositely oriented toroidal field which is either intermittently mixed with the dominant field, or resides in a different layer. In view of this controversy, it is worth considering the implications of our findings reported in Section 3.4 for the issue of the origin of anti-Hale regions.

Our findings regarding non-Hale regions can be summarized in the following.

- There is a clear excess of non-Hale regions at low tilts (here called anti-Hale regions).
- These anti-Hale regions share the same or very similar A – Φ and d – Φ scalings, as well as the same latitude–time distribution (butterfly diagram) as Hale regions and other non-Hale regions.
- The tilt distribution of anti-Hales and non-Hales shows no indication of any mean tilt, and it definitely does not follow Joy’s law.
- There is a curious pattern of differences in flux and pole separation between anti-Hale flipped Hale and Hale regions, discussed in Section 3.4 above.

These findings suggest that there is little physical difference between anti-Hale regions and flipped Hale regions, apart from some size trends and from the numerical excess in the number of anti-Hales. And the only significant physical difference between Hales and flipped Hales, the lack of tilt in non-Hales, is already reflected in a tendency, noted in Section 3.3, of high-tilt Hale regions to be oblivious of Joy’s law. There should be therefore a simple physical sequence

$$\text{Hale} \Rightarrow \text{high-tilt Hale} \Rightarrow \text{high-tilt non-Hale} \Rightarrow \text{anti-Hale}$$

reflecting an increasing amount of writhe in the 3D structure of the emerging flux loop. The leptokurtic character of the observed tilt distribution suggests that the large degree of writhe underlying the three categories on the right side of the above scheme is due to a small fraction of AR flux loops being subjected to an intermittent large-amplitude torque for some length of time τ during their rise. A plausible (though not the only possible) source for such torque is if the rising flux loop is caught in a large-scale vortex in the convective zone. The increase of the writhe will then stop after time τ , so the observed tilt will be primarily determined by the probability distribution of the length τ of such intermittent events and by the magnetic tension in the flux loop resisting the torque. When the angle of the writhe exceeds 90° degrees, a non-Hale region is observed, while when the angle approaches 180° degrees, an anti-Hale AR emerges (Fig. 14).

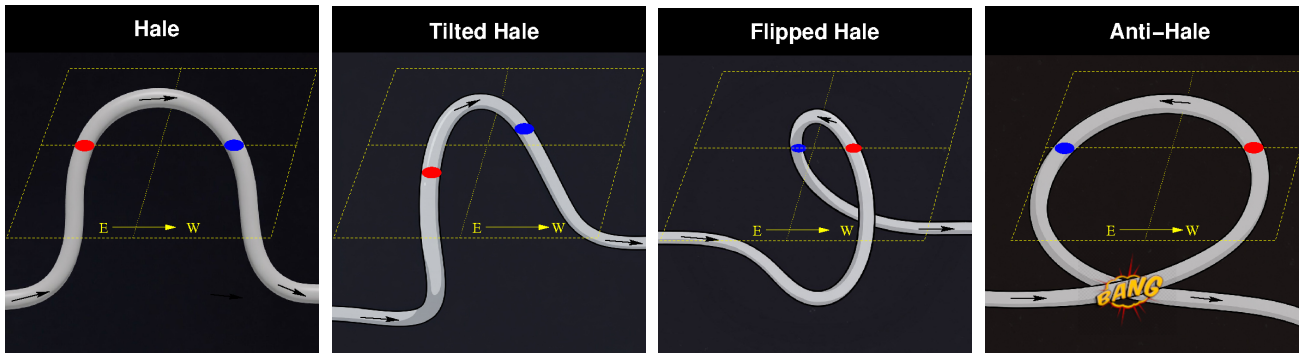


Fig. 14. The Hale—anti-Hale sequence. Cartoon illustrating the suggested subsurface magnetic structures underlying each tilt category

The excess number of anti-Hale regions is rather naturally explained in this scenario as a simple mechanical effect. Once the angle of the writhe approaches 180° , the legs of the flux loop will bump into each other, and the loop's resistance against further distortion will greatly increase due to the freezing-in condition. Hence, if the applied torque is constant, further increase of the writhe will be much slower (or may even asymptotically stop) near writhe angles of 180° . Then, for perturbations with a lifetime τ exceeding a threshold value, practically all rising flux loops will end up as anti-Hales, leading to an excess in this tilt range.

The end points of the above sequence then correspond to a simple Ω -loop (Hale regions) and a full, curled Ω -loop or ‘XO-loop’ (anti-Hale regions). The increasing degree of writhe between the two extremes corresponds to the high-tilt transitional states.

We believe that this scenario offers a simple and natural framework in which all the empirical findings listed above seamlessly fit. Indeed: the resistance of the loop to distortion is due to the curvature force, scaling as B^2/d , while the external drag scales with the inverse of the tube diameter, as $(B/\Phi)^{1/2}$. Hence, resistance against the drag increases with $B^{3/2}\Phi^{1/2}/d$. The most extreme writhe angles near 180° will be reached preferentially by loops with lower resistance, i.e. lower flux and higher pole separation. This is exactly the trend shown by anti-Hales relative to higher-tilt non-Hale ARs (Table 2).

4.3. Implications for active region formation

Models and concepts for the subsurface origin of active regions are reviewed by Fan (2021) and Weber et al. (2023). The classic paradigm of the buoyant rise of a flux loop from the bottom of the convective zone to near-surface layers is still the only coherent scenario (Petrovay & Christensen 2010) worked out in numerical detail. Alternative possibilities include originating depths in the bulk of the convection zone or in the near-surface shear layer, and rise driven by the drag of convective upflows (see, e.g., Birch et al. 2016, Hotta & Iijima 2020 and Chen et al. 2022).

Predictions of AR scaling laws from these models have focused on Joy’s law. Suggestions for the origin of this law include the following.

- (1) The tilt may reflect the orientation of the underlying flux tubes giving rise to the emerging loops. The orientation of these tubes, originating from the windup of the seed poloidal field present at solar minimum, may be inclined to the azimuthal direction. (Babcock 1961; Norton & Gilman 2005; Tlatova et al. 2018)

- (2) The tilt forms during the rise of the flux loop through the convective zone due to the action of Coriolis force on
 - flows inside the loop whose rise is driven by magnetic buoyancy (D’Silva & Choudhuri 1993; Caligari et al. 1995; Weber et al. 2013 etc.)
 - helical convective flows distorting the loop (and possibly contributing to its rise) via the drag (“ Σ -effect”, Longcope et al. 1998)
- (3) The tilt may form during and/or after the emergence of the flux loop through the surface, due to the effect of supergranular flows affected by the Coriolis force (Roland-Batty et al. 2025, Schunker & K V 2025).

If our above scenario for the origin of anti-Hale ARs is correct, the excess in the tilt angle of non-Hale regions should be observed around the position angle of the underlying horizontal flux tubes, as this determines the writhe angle where the loop legs will collide. The lack of tilt in anti-Hale ARs may then be considered as evidence against the scenario (1). On the other hand, irrespective of the origin of anti-Hale ARs, the fact that a well-defined subset of ARs does not display any tilt seems to contradict scenario (3), which should act on all loops emerging through the solar surface, irrespective of magnetic orientation. Our findings on non-Hale active regions therefore seem to support scenario (2), implying that active region flux loops originate from the deep convective zone and their shape is primarily determined before they emerge. The majority of observations of the evolution of AR tilts also support this scenario (Kosovichev & Stenflo 2008; Sreedevi et al. 2024, 2025).

In the classic model of the origin of ARs, sometimes called the “buoyant thin flux tube paradigm”, the underlying toroidal field lies in the tachocline, at or slightly below the bottom of the convective zone. In such models several independent lines of evidence point to an initial field strength of $B_0 \sim 10^5$ G (see Petrovay & Christensen 2010 for a summary of these arguments). The prediction by such models (Fan et al. 1994) for the tilt is $\gamma_J \sim \Phi^{1/4} B_0^{-5/4}$. Finding evidence for this dependence would be a decisive “smoking gun” in favour of the thin flux tube model. However, as we have seen in Section 3.3, the observed flux dependence of the tilt is much weaker than the predicted $\Phi^{1/4}$ dependence. This is not necessarily in contradiction with the classic model as the initial field strength may also vary, and there may well be a statistical relation between Φ and B_0 . Indeed, as discussed in Section 3.1 above, our A – Φ relation implies such a relation between the flux of an AR and its mean magnetic field in the photospheric layers.

On the other hand, the pole separation d has received little attention in previous considerations on the origin of ARs. Ob-

servations of AR evolution generally indicate that after an initial rapid increase, d saturates at a constant value of ~ 100 Mm (Kosovichev & Stenflo 2008; Schunker et al. 2019; Švanda et al. 2025). Indeed, recurrent sunspot groups are often seen to return several times with the position of the polarities hardly changing at all. This is a surprising fact in the light of the buoyant flux loop paradigm as the most unstable modes tend to be those with low wavenumber m , corresponding to scales of 300 Mm or longer. The observed length scales lie closer to the scales of turbulent convection in the deep convective zone in mixing-length models and numerical simulations, determined by the scale height. It may then be that the typical scale of finite amplitude initial perturbations plays a more important role in determining the size of the rising flux loops. The puzzling but very robust logarithmic scaling of d with Φ discovered in our analysis may hold important clues regarding turbulence spectra in the deep convective zone and originating depths of the rising flux loops.

5. Conclusion

In this paper we have analyzed the recently compiled ARISE database of solar bipolar magnetic regions to study how other AR parameters scale with the fundamental parameter, the magnetic flux Φ . The other parameters studied were the area A , the pole separation d and the tilt angle γ_J .

Our most novel finding is that, contrary to what was found (or rather, a priori assumed) in earlier studies the d – Φ relation is not a power law but a well determined and highly robust logarithmic relation. The scaling of A with Φ is found to deviate from linear, implying that the mean field strength increases with region size. For the tilt angle we find that the slope of Joy’s law shows a tendency to increase with Φ but the significance of this result is low and the trend is much weaker than the theoretical prediction $\gamma_J \sim \Phi^{1/4}$. Scatter around Joy’s law decreases linearly with Φ and exponentially with d .

The distribution of residuals around the mean scaling laws was also studied. A and d were found to be roughly lognormally distributed, while we confirm the earlier finding that residuals from Joy’s law follow Student’s t -distribution with ~ 3.5 degrees of freedom. These scalings and residual distributions allow us to construct a recipe for the synthesis of an ensemble or population of active regions correctly reflecting the observed statistics. Collecting the relevant fitting formulae from the main text of the paper, this recipe is summarized in the Appendix.

Non-Hale active regions were also studied as a separate set. We confirm that their tilt angle distribution shows a significant excess at low tilts (anti-Hale ARs). In contrast to earlier studies we show that neither the anti-Hale ARs nor non-Hales in general follow Joy’s law: instead, their tilt angle distribution is best represented by vanishing mean tilt. At the same time, anti-Hales follow the same or nearly the same A – Φ and d – Φ scaling laws as Hale regions; their distribution on the butterfly diagram also agrees with the general population.

From these findings we infer that Hale, non-Hale and anti-Hale ARs all originate from the same rising flux loops, a small fraction of which is intermittently subjected to an unusually strong torque during their rise, increasing their writhe. Non-Hales are thus essentially flipped Hale regions. The excess anti-Hale population is likely due to the fact that for a writhe approaching 180° the loop legs come in contact, freezing in will tend to impede further twisting, hence perturbations lasting longer than a threshold will all result in a nearly azimuthal alignment of the polarities.

Implications of our findings for the subsurface motion and origin of AR flux loops were also discussed. These results are most easily reconciled with a scenario where the toroidal field resides in the deep convective zone or below, and turbulent perturbations form finite amplitude loops from this field. These loops rise towards the surface under the action of buoyancy and/or external upflows, gaining tilt under the action of the Coriolis force. A small fraction is subjected to extreme, intermittent perturbations resulting in either very large tilts or anti-Hale orientation.

Acknowledgements. This research was supported by the European Union’s Horizon 2020 research and innovation programme under grant agreement No. 955620 and by the NKFIH excellence grant TKP2021-NKTA-64. RE is also grateful to the Hungarian National Research, Development and Innovation Fund (NKFIH, grant no. K142987); the UK Science and Technology Facilities Council (STFC, grant no. ST/M000826/1); PIFI (China, grant no. 2024PVA0043).

References

Babcock, H. W. 1961, *ApJ*, 133, 572
 Birch, A. C., Schunker, H., Braun, D. C., et al. 2016, *Science Advances*, 2, e1600557
 Caligari, P., Moreno-Insertis, F., & Schussler, M. 1995, *ApJ*, 441, 886
 Cameron, R. H. & Schüssler, M. 2016, *A&A*, 591, A46
 Chen, F., Rempel, M., & Fan, Y. 2022, *ApJ*, 937, 91
 D’Silva, S. & Choudhuri, A. R. 1993, *A&A*, 272, 621
 D’Silva, S. & Howard, R. F. 1993, *Sol. Phys.*, 148, 1
 Erofeev, D. V. & Erofeeva, A. V. 2023, *Geomagnetism and Aeronomy*, 63, 1007
 Fan, Y. 2021, *Living Reviews in Solar Physics*, 18, 5
 Fan, Y., Fisher, G. H., & McClymont, A. N. 1994, *ApJ*, 436, 907
 Fisher, G. H., Fan, Y., & Howard, R. F. 1995, *ApJ*, 438, 463
 Forgács-Dajka, E., Dobos, L., & Ballai, I. 2021, *A&A*, 653, A50
 Harvey, K. L. & Zwaan, C. 1993, *Sol. Phys.*, 148, 85
 Hotta, H. & Iijima, H. 2020, *MNRAS*, 494, 2523
 Jha, B. K., Karak, B. B., Mandal, S., & Banerjee, D. 2020, *ApJ*, 889, L19
 Kosovichev, A. G. & Stenflo, J. O. 2008, *ApJ*, 688, L115
 Lemerle, A., Charbonneau, P., & Carignan-Dugas, A. 2015, *ApJ*, 810, 78
 Leussu, R., Usoskin, I. G., Senthamizh Pavai, V., et al. 2017, *A&A*, 599, A131
 Li, J. 2018, *ApJ*, 867, 89
 Longcope, D. W., Fisher, G. H., & Pevtsov, A. A. 1998, *ApJ*, 507, 417
 McClintock, B. H. & Norton, A. A. 2013, *Sol. Phys.*, 287, 215
 McClintock, B. H. & Norton, A. A. 2016, *ApJ*, 818, 7
 McClintock, B. H., Norton, A. A., & Li, J. 2014, *ApJ*, 797, 130
 Meunier, N. 2003, *A&A*, 405, 1107
 Muñoz-Jaramillo, A., Navarrete, B., & Campusano, L. E. 2021, *ApJ*, 920, 31
 Muñoz-Jaramillo, A., Senkpiel, R. R., Windmueller, J. C., et al. 2015, *ApJ*, 800, 48
 Muraközy, J. 2024, *A&A*, 690, A257
 Norton, A. A. & Gilman, P. A. 2005, *ApJ*, 630, 1194
 Petrovay, K. 2020, *Living Reviews in Solar Physics*, 17, 2
 Petrovay, K. & Christensen, U. R. 2010, *Space Sci. Rev.*, 155, 371
 Poisson, M., Démoulin, P., Mandrini, C. H., & López Fuentes, M. C. 2020, *ApJ*, 894, 131
 Qin, L., Jiang, J., & Wang, R. 2025, *ApJ*, 986, 114
 Roland-Batty, W., Schunker, H., Cameron, R. H., et al. 2025, *A&A*, 700, A28

Schunker, H., Baumgartner, C., Birch, A. C., et al. 2020, A&A, 640, A116

Schunker, H., Birch, A. C., Cameron, R. H., et al. 2019, A&A, 625, A53

Schunker, H. & K V, A. L. 2025, Sol. Phys., 300, 161

Seiden, P. E. & Wentzel, D. G. 1996, ApJ, 460, 522

Sheeley, Jr., N. R. 1966, ApJ, 144, 723

Sreedevi, A., Jha, B. K., Karak, B. B., & Banerjee, D. 2023, ApJS, 268, 58

Sreedevi, A., Jha, B. K., Karak, B. B., & Banerjee, D. 2024, ApJ, 966, 112

Sreedevi, A., Karak, B. B., Jha, B. K., Gupta, R., & Banerjee, D. 2025, ApJ, 994, L40

Stenflo, J. O. & Kosovichev, A. G. 2012, ApJ, 745, 129

Tian, L., Liu, Y., & Wang, H. 2003, Sol. Phys., 215, 281

Tlatova, K., Tlatov, A., Pevtsov, A., et al. 2018, Sol. Phys., 293, 118

van Driel-Gesztelyi, L. & Green, L. M. 2015, Living Reviews in Solar Physics, 12, 1

Švanda, M., Jurčák, J., & Schmassmann, M. 2025, A&A, 700, A40

Wang, R., Jiang, J., & Luo, Y. 2023, ApJS, 268, 55

Wang, R., Jiang, J., & Luo, Y. 2024, ApJ, 971, 110

Wang, Y. M., Colaninno, R. C., Baranyi, T., & Li, J. 2015, ApJ, 798, 50

Wang, Y. M. & Sheeley, Jr., N. R. 1989, Sol. Phys., 124, 81

Weber, M. A., Fan, Y., & Miesch, M. S. 2013, Sol. Phys., 287, 239

Weber, M. A., Schunker, H., Jouve, L., & Işık, E. 2023, Space Sci. Rev., 219, 63

Will, L. W., Norton, A. A., & Hoeksema, J. T. 2024, ApJ, 976, 20

Yeates, A. R., Cheung, M. C. M., Jiang, J., Petrovay, K., & Wang, Y.-M. 2023, Space Sci. Rev., 219, 31

Zeng, S.-G., Zhao, A.-Y., Yi, S., et al. 2024, ApJ, 975, 210

Appendix A: Active region population synthesis: a recipe

Surface flux transport models, widely used to compute the evolution of the Sun's large scale magnetic field, include ARs as a source term (Yeates et al. 2023). This source often needs to be modelled to account for missing data or future evolution: it is clearly important for any such model to be as realistic as possible.

In what follows we give a concise summary of the relevant findings in our paper in the form of a “recipe” to generate an ensemble of active regions to be used as source term in an SFT or dynamo model. Prescribing when, where and with what magnetic flux a bipolar region will emerge in such models is beyond the scope of the present work. We restrict our attention to determining the area A of the individual flux patches; their separation d ; and the tilt angle of the bipole axis.

For a bipolar region of magnetic flux Φ emerging at latitude λ :

(1) The logarithm of the area A of the individual polarity patches is best represented as $\log A = \langle \log A \rangle + r_A$ where

$$\langle \log A[\text{MSH}] \rangle = k \log \Phi[\text{Mx}] + \log C_A \quad (\text{A.1})$$

with $k = 0.84$ and $C_A = 6.17 \cdot 10^{-16}$, while r_A is a Gaussian random variable with standard deviation 0.1.

(2) The pole separation may be best represented as $d = r_d \cdot \langle d \rangle$ where

$$\langle d \rangle = m_d \log(\Phi/\Phi_0) \quad (\text{A.2})$$

with $m_d = 3^\circ 32$ and $\Phi_0 = 1.6 \cdot 10^{20} \text{ Mx}$, while $\log(r_d)$ is a normally distributed random variable, with standard deviation 0.41.

(3) The tilt angle γ_J is best represented as $\langle \gamma_J \rangle + r_J \sigma_J$ where

$$\langle \gamma_J \rangle = m_J \sin \lambda \quad m_J = 28^\circ 62 \quad (\text{A.3})$$

while r_J is a random variable with a distribution described by Student's t -distribution of 3.7 degrees of freedom, and σ_J is obtained from

$$\sigma_J = \sigma_\infty + A \exp(-d/d_0) \quad \text{with} \quad (\text{A.4})$$

$$\sigma_\infty = 11^\circ 0 \quad A = 33^\circ 5 \quad d_0 = 4^\circ 4$$

or alternately from

$$\sigma_J = a + b \log(\Phi[\text{SFU}]) \quad \text{with} \quad (\text{A.5})$$

$$a = 25^\circ 57 \quad \text{and} \quad b = 3^\circ 75$$

in which case a t -function with 2.9 degrees of freedom is to be used.

For applications where an accurate representation of the tails of the distribution matters, accounting for the skewness by suppressing [amplifying] the positive [negative] tail of the distribution may be considered. With this correction, the distribution will correctly represent the majority of non-Hale ARs with the exception of the excess of anti-Hale regions (comprising $\sim 1\%$ of all ARs).